RESEARCH ARTICLE SUMMARY

CELL BIOLOGY

The nucleus measures shape changes for cellular proprioception to control dynamic cell behavior

Valeria Venturini, Fabio Pezzano, Frederic Català Castro, Hanna-Maria Häkkinen, Senda Jiménez-Delgado, Mariona Colomer-Rosell, Monica Marro, Queralt Tolosa-Ramon, Sonia Paz-López, Miguel A. Valverde, Julian Weghuber, Pablo Loza-Alvarez, Michael Krieg, Stefan Wieser*, Verena Ruprecht*

INTRODUCTION: Human beings are equipped with multiple senses (sight, hearing, smell, taste, touch, and proprioception) to help them to react properly to their environment. The human body is composed of trillions of cells that similarly require multiple sensations to fulfill their task in specific tissues. From a cellular perspective, the three-dimensional (3D) tissue microenvironment is a crowded place in which cells experience a multitude of physical constraints and mechanical forces. These conditions can lead to cell shape changes—for example, as observed when motile cells squeeze through tight spaces or when cells deform in densely packed tissue regions. To guarantee tissue integrity and homeostasis, cells need to be able to respond to these mechanical challenges in their tissue microenvironment, both in the adult organism and during embryonic development. How cells can measure their own shape and adapt their dynamic behavior to the physical surroundings remains an open question.

RATIONALE: The actomyosin cytoskeleton is a structural scaffold within cells that controls mechanical cell properties and dynamic cellular processes such as cell migration. Cytoskeletal networks can contract and thereby generate force by using the activity of myosin II motor proteins. Cell contractility influences the mode and speed of cell migration. Various cell types have been observed to switch to a highly contractile and fast amoeboid cell migration type in constrained environments. This suggests the presence of a conserved mechanosensitive pathway capable of translating mechanical cell deformations into adaptive cytoskeletal arrangements that allow cells to react dynamically to changes in their tissue microenvironment.

RESULTS: Here, we show that the nucleus, the biggest organelle in the cell, translates cell shape changes into a deformation signal regulating cell behavior. We found that variable cell squeezing defines the specific set point of cell contractility, with increased cell deformation leading to higher cortical myosin II levels and promoting fast amoeboid cell migration. This adaptive cellular response to deformation was rapid (<1 min), stable over time (>60 min), and reversible upon confinement release. We found that changes in cell behavior were associated with nucleus stretch and unfolding of the inner nuclear membrane (INM), supporting the idea that the nucleus functions as a fast mechanical responder for sensing cell shape variations. We show that INM unfolding triggered a calcium-dependent mechanotransduction pathway via the activation of cytosolic phospholipase A2 ($cPLA_2$) and metabolite production of arachidonic acid (AA) that regulates myosin II activity. This establishes the nucleus as an intracellular mechano-gauge that measures shape deformations and directly controls morphodynamic cell behavior. Furthermore, we found that the combination of nuclear deformation and intracellular calcium levels, regulated by nuclear positioning, allows cells to distinguish distinct shape deformations and adapt their behavior to changing tissue microenvironments.

CONCLUSION: Here, we show that the nucleus acts as a central hub for cellular proprioception, which, in a manner similar to how we sense our body posture and movement, enables single cells to precisely interpret and respond to changes in their 3D shape. The rapid increase in cell contractility and migration competence upon cell squeezing equips cells with a rapid "evasion reflex": In constrained environments, cells polarize and acquire a rapid migratory phenotype that enables cells to move away and squeeze out from tight spaces or crowded tissue regions. The nucleus thus allows cells to decode changes in their shape and to adjust their behavior to variable tissue niches, relevant for healthy and pathological conditions. ■

The list of author affiliations is available in the full article online.
*Corresponding author. Email: stefan.wieser@icfo.eu (S.W.); verena.ruprecht@crg.eu (V.R.)
Cite this article as V. Venturini *et al.*, *Science* **370**, eaba2644 (2020). DOI: 10.1126/science.aba2644

READ THE FULL ARTICLE AT
https://doi.org/10.1126/science.aba2644

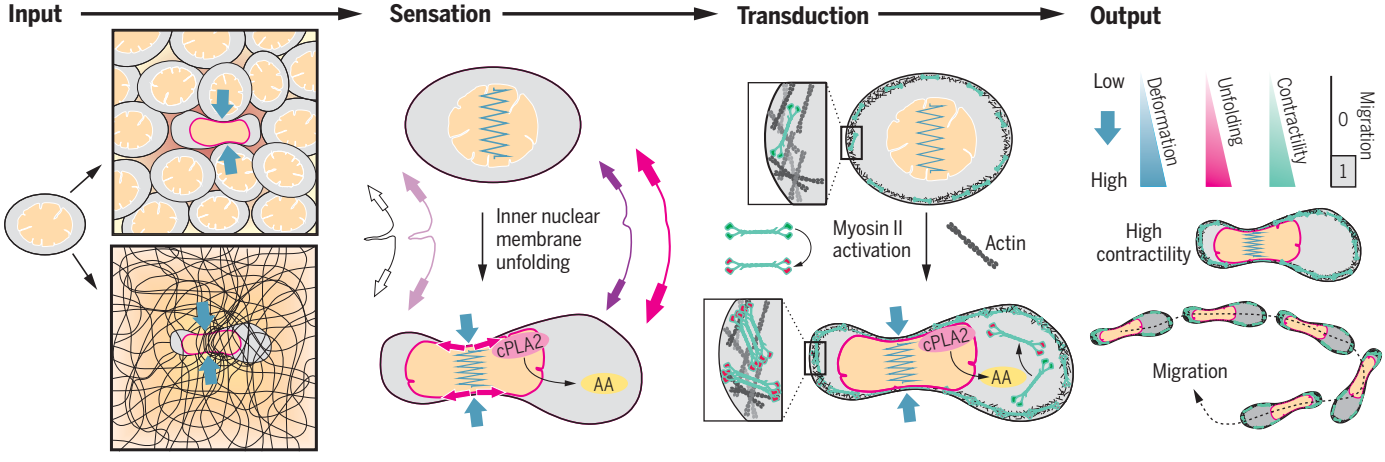

The nucleus acts as an elastic mechanotransducer of cellular shape deformation and controls dynamic behavior. Cell shape changes induce inner nuclear membrane unfolding and activation of the $cPLA_2$-AA pathway. This transduces mechanical nucleus stretch into myosin II recruitment to the cell cortex regulating actin cytoskeleton contractility and cellular behavior. High contractility levels further lead to motile cell transformation and initiate amoeboid cell migration.

RESEARCH ARTICLE

CELL BIOLOGY

The nucleus measures shape changes for cellular proprioception to control dynamic cell behavior

Valeria Venturini[1,2], Fabio Pezzano[2], Frederic Català Castro[1], Hanna-Maria Häkkinen[2], Senda Jiménez-Delgado[2], Mariona Colomer-Rosell[1], Monica Marro[1], Queralt Tolosa-Ramon[2], Sonia Paz-López[3], Miguel A. Valverde[3], Julian Weghuber[4], Pablo Loza-Alvarez[1], Michael Krieg[1], Stefan Wieser[1]*, Verena Ruprecht[2,5]*

The physical microenvironment regulates cell behavior during tissue development and homeostasis. How single cells decode information about their geometrical shape under mechanical stress and physical space constraints within tissues remains largely unknown. Here, using a zebrafish model, we show that the nucleus, the biggest cellular organelle, functions as an elastic deformation gauge that enables cells to measure cell shape deformations. Inner nuclear membrane unfolding upon nucleus stretching provides physical information on cellular shape changes and adaptively activates a calcium-dependent mechanotransduction pathway, controlling actomyosin contractility and migration plasticity. Our data support that the nucleus establishes a functional module for cellular proprioception that enables cells to sense shape variations for adapting cellular behavior to their microenvironment.

The three-dimensional (3D) shape of an organism is built by active force-generating processes at the cellular level and the spatiotemporal coordination of morphodynamic cell behavior. Contractility of the actomyosin cell cortex represents a major cellular force production mechanism underlying cellular shape change (*1*), cell polarization (*2*), and active cell migration dynamics (*3*). Contractility levels are regulated by the activity of nonmuscle myosin II motor proteins (*4*) and are precisely controlled to tune single-cell and tissue morphodynamics during development (*5*, *6*) and tissue homeostasis and disease in the adult organism (*7*, *8*). Still, mechanisms that regulate the set-point level of cortical contractility on the single-cell level remain poorly understood.

To adjust cortical contractility levels, cells need to make quantitative measures of their mechanochemical 3D tissue microenvironment and translate this information into a defined morphodynamic output response. Morphogens that act as chemical information carriers during embryogenesis have attracted major attention (*9*), modulating cytoskeletal and cellular dynamics via receptor signaling pathways that tune protein activities (such as phosphorylation states) and/or protein expression levels. In contrast, physical parameters of the 3D tissue niche and mechanical forces gain importance as regulators of cellular morphodynamics and myosin II–dependent cortical contractility levels (*10*, *11*). In vivo, mechanical cell deformation and cellular packing density in crowded tissue regions has been shown to influence major morphodynamic processes such as cortical actomyosin contractility (*12*, *13*), cell division (*14*–*17*), and cell extrusion and invasion (*18*). Ex vivo studies have provided further evidence on the single-cell level that physical cell deformation is sufficient to modulate cortical myosin II localization and motor protein activity (*19*, *20*) and influence morphodynamic cell behavior (*21*, *22*).

A recent example is the identification of a fast amoeboid migration mode, called stable-bleb migration, that is triggered by an increase in cortical contractility via genetic or physical cell perturbation (*23*). This morphodynamic migration switch was shown to be present in both undifferentiated and lineage-committed embryonic progenitor cells and was also identified in various other cell types (*24*–*29*). This finding suggests that a conserved, albeit unknown, mechanosensitive cellular signaling module regulates myosin II–based cortical contractility and motile cell transformation depending on cellular shape deformations in constrained tissue microenvironments.

Cell contractility levels increase upon cell confinement and regulate migration plasticity

To approach the question of how cells can measure and adaptively respond to physical cell shape changes within their 3D tissue microenvironments, we established a synthetic approach that enables the mimicking of mechanical cell deformations in controlled 3D microconfinement assays (*30*). Primary progenitor stem cells were isolated from blastula stage zebrafish embryos and cultured in planar confinement assays of defined height to mimic various cell deformation amplitudes (fig. S1A). Lowering confinement height in discrete steps increased cell deformation, which scaled nonlinearly with a pronounced enrichment of myosin II at the cell cortex relative to cortical actin accumulation (Fig. 1, A and B; fig. S1, B to D; and movie S1). Cortical accumulation of myosin II was accompanied by an increase in cellular bleb size (fig. S1E and movie S1), indicative of an active increase in cortical contractility levels depending on confinement height. Myosin II relocalization to the cell cortex in confined cells was rapid [half-time ($t_{1/2}$) < 1 min] (Fig. 1, C and D) and temporally stable under confinement. Distinct plateaus of cortical myosin II enrichment were evident, with myosin II relocalization increasing for larger cell deformations (Fig. 1C). A cell confinement height smaller than 7 μm caused a pronounced increase in cell lysis during compression, defining a maximal threshold deformation of ~30% of the initial cell diameter (d), given a blastula cell size of d ~ 25 μm (fig. S3H). Overall, these data support that the physical microenvironment defines a specific set-point level of cortical contractility as a function of cell deformation.

We have previously shown that an increase in myosin II–mediated cortical contractility induced a stochastic motility switch into a highly motile amoeboid migration phenotype called stable-bleb mode (*23*). In accordance with these results, rapid cortical myosin II enrichment in confinement resulted in spontaneous cell polarization which initiated amoeboid cell migration (Fig. 1, E and F; fig. S1, F and G; and movies S2 and S3). Polarized cells revealed characteristic actomyosin density gradients from the cell front toward the rear, accompanied by fast retrograde cortical flows (fig. S1H and movies S2 and S3); these cortical flows have been shown to power fast amoeboid migration in polarized cells (*23*, *31*). Meanwhile, unpolarized cells showed random tumbling with minimal net translocation (figs. S1, F and G, and S2A). These data support that physical cell deformation in confinement is sufficient to increase actomyosin network contractility and trigger rapid amoeboid cell migration.

Release of cell compression induced a rapid relocalization of cortical myosin to the cytoplasm (Fig. 1G and fig. S1I), followed by a rapid loss of cell polarization and related migratory capacity (fig. S1G and movie S4). Interfering with myosin II activity via blebbistatin inhibited cell polarization and associated cell motility in confinement (Fig. 1E and fig. S1J), in accordance with a necessary role of myosin II–based contractility in cell polarization and

[1]ICFO – Institut de Ciències Fotòniques, The Barcelona Institute of Science and Technology, 08860 Castelldefels, Spain. [2]Centre for Genomic Regulation (CRG), The Barcelona Institute of Science and Technology, 08003 Barcelona, Spain. [3]Laboratory of Molecular Physiology, Department of Experimental and Health Sciences, Universitat Pompeu Fabra (UPF), Barcelona, Spain. [4]School of Engineering, University of Applied Sciences Upper Austria, Stelzhamerstraße 23, Wels 4600, Austria [5]Department of Experimental and Health Sciences, Universitat Pompeu Fabra (UPF), Barcelona, Spain
*Corresponding author. Email: stefan.wieser@icfo.eu (S.W.); verena.ruprecht@crg.eu (V.R.)

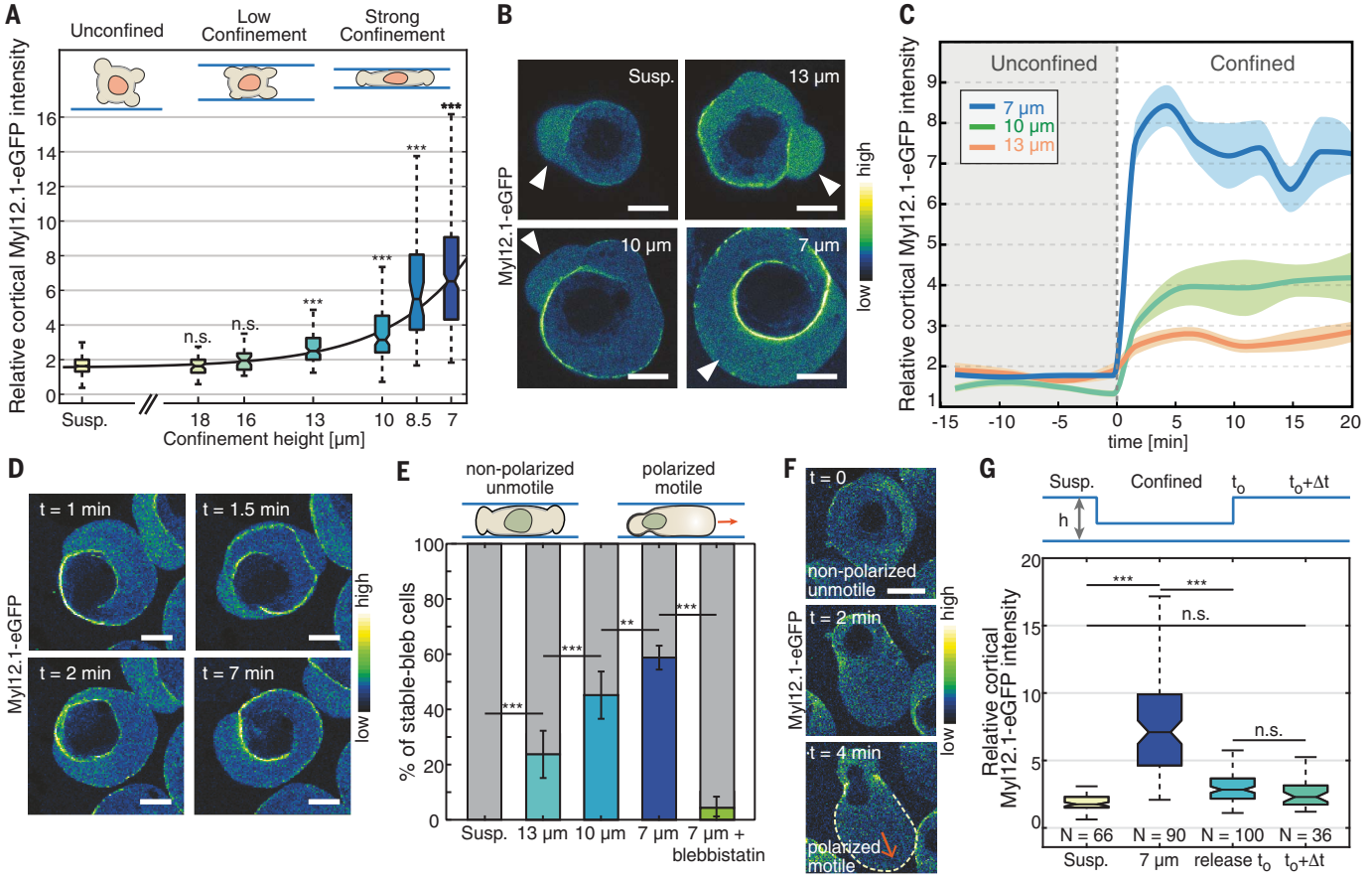

Fig. 1. Cell deformation in confined environments defines cell contractility, polarization, and fast amoeboid cell migration. (**A**) Relative cortical myosin II enrichment for decreasing confinement height in unpolarized progenitor cells [N = 477 cells (suspension, unconfined); N = 56 (18 μm); N = 35 (16 μm); N = 103 (13 μm); N = 131 (10 μm); N = 49 (8.5 μm); N = 348 (7 μm)]. Significance values are with respect to the suspension condition. Black line shows a monoexponential fit with offset to the data. (**B**) Exemplary confocal fluorescence images of control progenitor stem cells in suspension (Susp.) and indicated confinement heights expressing Myl12.1-eGFP (myosin II). White arrows point to cellular blebs. (**C**) Temporal dynamics of cortical myosin II recruitment upon mechanical confinement at time (t) = 0 at the indicated heights. Thick lines correspond to the mean, and areas correspond to the standard error of the mean (SEM). N > 50 cells for all conditions. (**D**) Exemplary cross-sectional time-lapse images of myosin II–eGFP–expressing cells under 7 μm confinement. (**E**) Percentage of polarized motile stable-bleb cells in suspension at indicated confinement heights and myosin II inhibition (blebbistatin) at 7 μm (each N > 500). (**F**) Representative time-lapse images of a myosin II–eGFP–expressing cell undergoing spontaneous stable-bleb cell polarization and migration initiation. Dashed line shows the stable-bleb cell front and red arrow points in the direction of movement. (**G**) Relative cortical myosin II enrichment during reversible cell confinement. Cells were confined for 15 min before confinement was released, and cortical myosin II levels were measured at t_0 (0 to 5 min) and at $t_0 + \Delta t$ (30 to 60 min) after release. h, height. ***P < 0.0001, **P < 0.001; n.s., not significant. All scale bars, 10 μm.

migration induced by mechanical cell shape deformation. Cortical myosin II enrichment and cell polarization occurred independently of caspase activation (fig. S1K), supporting that morphodynamic changes are not caused by the activation of proapoptotic signaling programs. Furthermore, transcriptional inhibition did not block cortical myosin II relocalization and cell polarization (fig. S1L), indicating that a nongenetic program is regulating cellular morphodynamics under cell compression.

During gastrulation, blastoderm embryonic progenitor stem cells specify into different lineages (ectoderm, mesoderm, endoderm) and acquire distinct biomechanical and morphodynamic characteristics, driving germ layer positioning and shape formation of the embryo (*32*, *33*) (Fig. 2, A and B). To test the mechanosensitive response to cell deformation at later developmental stages, we obtained different progenitor cell types from embryos via genetic induction or using endogenous reporter lines. Under confinement, nonmotile ectodermal cells rapidly polarized and started to migrate in an amoeboid stable-bleb mode. Similarly, mesendodermal cells underwent a fast mesenchymal-to-amoeboid transition in confinement (Fig. 2, B to D; fig. S2A; and movies S3 and S5). The fraction of polarized stable-bleb cells and their cell speed were comparable for different progenitor cell types in confinement (fig. S2, B and C). Together, these results support that physical cell shape deformation in confined tissue microenvironments activates a mechanosensitive signaling pathway regulating adaptive cortical contractility levels and morphodynamic migration plasticity in pluripotent and lineage-committed embryonic stem cells.

The cell nucleus is a mechanosensor of large cell shape deformation

We next sought to identify potential mechanisms that control cellular shape deformation sensing and adaptive morphodynamic behavior. Cortical myosin II relocalization and amoeboid cell transformation occurred on passivated confinement surfaces independently of adhesive substrate coating (figs. S2, A and C, and S3A) and cell-cell contact formation (fig. S3B). These observations support that the activation of cortical contractility in confinement occurs independently of adhesion-dependent

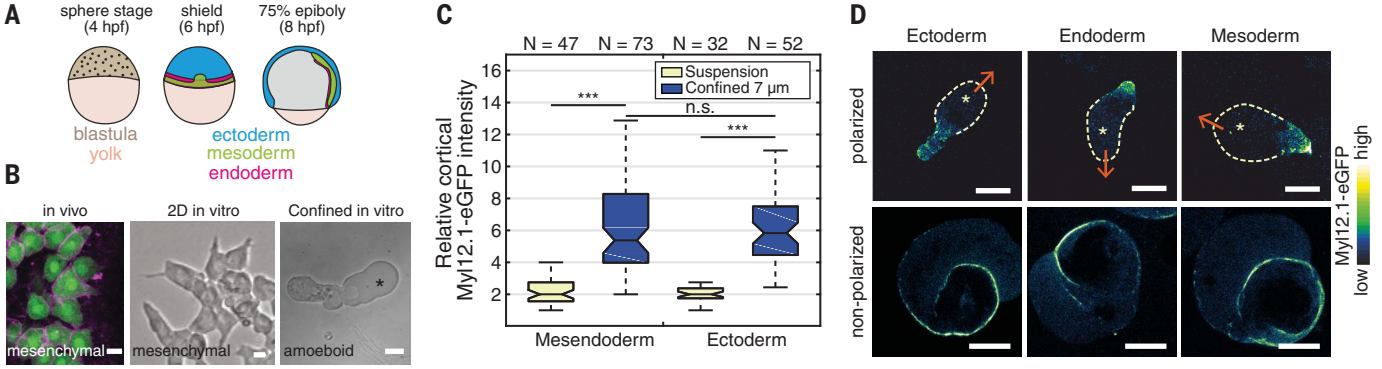

Fig. 2. Physical confinement triggers amoeboid migration in different cell lineages. (**A**) Sketch of the developing zebrafish embryo at sphere [4 hours post-fertilization (hpf)], shield (6 hpf), and 75% epiboly (8 hpf) stage. (**B**) Exemplary confocal and bright-field images of mesodermal cells in vivo expressing Lyn-Tomato (magenta, membrane) and GFP (green) under the mezzo promoter (left), induced mesendodermal cells in vitro plated on a 2D fibronectin-coated surface (middle), and under 7 µm confinement (right). Asterisk indicates stable-bleb cell front. (**C**) Relative cortical myosin II intensity for mesendodermal and ectodermal progenitor cells in control suspension and confinement conditions. (**D**) Exemplary confocal images of stable-bleb polarized (top) and nonpolarized (bottom) progenitor cell types expressing myosin II–eGFP under 7 µm confinement. From left to right: ectoderm, endoderm, and mesoderm cells. Dashed line and yellow asterisks indicate the stable-bleb cell front, and red arrows indicate the direction of cell migration. ***$P < 0.0001$. All scale bars, 10 µm.

mechanotransduction pathways (*34*). The temporal characteristics of myosin II relocalization dynamics in confined cells showing a fast, stable, and reversible accumulation of cortical myosin II (Fig. 1, C and D) suggested that shape deformation is sensed by a nondissipative cellular element that can rapidly measure and convert gradual cellular shape changes into stable contractility response levels.

The actomyosin cytoskeleton itself has been implicated to act as a mechanosensitive network (*20*), but it generally limits deformation sensing due to rapid turnover of the cell cortex (*35*). To test for the activation of mechanosensitive ion channels, we used gadolinium and GsMTx4, inhibitors of stretch-activated channels, with GsMTx4 having been shown to block the tension-dependent Piezo1 channel, which is activated after confinement of human cancer cells (*36*). Treatment with both inhibitors did not result in a significant reduction in cortical myosin II accumulation under cell deformation (fig. S3C), despite the presence of functional Piezo1 channels in these cells, as validated with the Piezo1-specific agonist Yoda (fig. S3D).

Notably, we observed that cortical myosin II enrichment only started to occur below a threshold confinement height (~13 µm) that correlated with the spatial dimension of the nucleus (Fig. 3A and fig. S3H). Analyzing nuclear shape change versus cortical myosin accumulation revealed a biphasic behavior, with a first phase in which the nucleus diameter remained nearly constant and no myosin II accumulation was observed, and a second phase in which the relative myosin accumulation linearly increased with the relative change in nucleus diameter (Fig. 3, A and B, and fig. S3E). In accordance with this observation, we expected a proportional change of nuclear surface ruffling upon deformation of an initially spherical nucleus. Measuring of nuclear surface folding by the expression of the inner nuclear membrane (INM) protein Lap2b-eGFP (enhanced green fluorescent protein–tagged lamina-associated polypeptide 2) revealed that membrane ruffling was continuously reduced when nucleus deformation started to occur at a threshold deformation of ~13 µm (Fig. 3, C to E; fig. S3F; and movie S6). In addition, analysis of nucleus membrane curvature for confined versus control cells in suspension indicated INM surface unfolding (Fig. 3, F and G, and movie S6), with no significant difference in total nuclear volume and surface (fig. S3G). Nucleus deformation further correlated with cortical myosin II accumulation in the endogenous in vivo context during the blastula-to-gastrula transition, when a gradient of cellular packing density appears from the animal pole toward the lateral margin (*37*) (fig. S2, D and E).

To further probe the dependence of cortical myosin II accumulation on nucleus size, we dissociated primary embryonic stem cells from early and late blastula stages, as cells reduce their size in consecutive rounds of early cleavage divisions (fig. S3H). Deforming cells of different sizes under similar confinement heights revealed that myosin II accumulation is correlated with relative changes in nucleus deformation but not cell deformation (Fig. 4, A and B). To test a functional role of the nucleus in regulating cortical contractility levels during cellular shape deformation, we analyzed cortical myosin II accumulation in mitotic cells that present a disassembled nuclear envelope. To arrest cells in mitosis and further increase the percentage of mitotic cells, we used nocodazole, a microtubule-disrupting drug. Confinement of mitotic cells (either spontaneous or nocodazole-induced) did not trigger a cortical myosin II accumulation at a 7 µm confinement height as it did in interphase blastula cells (Fig. 4C) or cell polarization (fig. S3I). However, mitotic cells did accumulate myosin II (Fig. 4D) and polarize (fig. S3I) in response to lysophosphatidic acid (LPA), a potent activator of Rho/Rho-associated coiled-coil containing protein kinase (ROCK) signaling, which has previously been shown to induce rapid cortical myosin II enrichment and amoeboid migration in zebrafish embryonic progenitor stem cells (*23*). During entry into mitosis, cells gradually lost cortical myosin II accumulations, which temporally correlated with the start of nuclear envelope breakdown (Fig. 4E). Altogether, these data show that myosin II enrichment is associated with nuclear shape deformation and stable INM membrane unfolding. This suggests that the nucleus functions as a continuous nondissipative sensor element of cell deformation involved in the mechanosensitive regulation of cortical contractility levels and cellular morphodynamics.

To directly test biophysical characteristics of the nucleus, we developed an assay to probe intracellular nucleus mechanics by optical tweezer measurements. For this purpose, latex beads of 1 µm size were injected into one-cell-stage embryos that dispersed across embryonic cells during early cleavage cycles and acted as intracellular force probes to measure rheological properties of the nucleus (fig. S4A). Trapezoidal loads were measured for cells in suspension and under 10-µm confinement (fig. S4, B to E). The recorded force followed the fast initial indentation to reach a peak force before it relaxed to a nonzero constant force-plateau. The relaxation time remained

unchanged between suspension (τ = 6.08 ± 1.1 s) and confined cells (τ = 4.00 ± 0.6 s) (fig. S4, D to H), suggesting a passive but rapid (second-scale) relaxation of a viscous component. The force-plateau on a long time scale corresponds to an elastic component of the nucleus (fig. S4I), in line with previous measurements that identified an elastic behavior of the nucleus (*38*) that can act as a cellular strain gauge. In addition, we observed that INM unfolding was stable over a measurement period of 60 min (fig. S4J) under mechanical cell deformation, supporting that INM stretch does not relax over extended time periods.

Nuclear deformation activates a calcium-dependent mechanotransduction pathway regulating myosin II activity

We next aimed to identify nucleus deformation–dependent signaling pathways that link the spatiotemporal correlation of nuclear shape changes with fast myosin II activation and changes in morphodynamic cell behavior. Our previous observations suggested that nucleus deformation and associated mechanosensitive processes at the INM interface are involved in the regulation of myosin II activity and cortical contractility. Among a set of molecules tested under confinement conditions (table S1), we identified cytosolic phospholipase A2 ($cPLA_2$) as a key molecular target mediating the activation of cortical myosin II enrichment (Fig. 5, A and B) and amoeboid cell transformation under cell compression (Fig. 5C). Inhibition of $cPLA_2$ by pharmacological interference using pyrrophenone robustly blocked cortical myosin II relocalization under varying confinement heights (fig. S5A). Furthermore, we observed a significant reduction of cortical myosin II levels in confined cells by morpholino (MO) interference with $cPLA_2$, while overexpression of $cPLA_2$ mRNA rescued the morphant phenotype and led to a myosin II accumulation comparable to that in control cells (Fig. 5, A and B). Residual myosin II activation in cells obtained from morphant embryos suggests a maternal contribution of $cPLA_2$ protein in the early embryo that cannot be targeted by MO interference. To exclude that other mechanisms, such as structural changes in the actin network, prevent cortical myosin II relocalization under $cPLA_2$ inhibition, we added LPA as an exogenous myosin II activator to $cPLA_2$ inhibited cells. Under this condition, myosin II was strongly accumulated at the cell cortex (fig. S5, B and C) and induced cell polarization associated with amoeboid motility (Fig. 5C). These data support that myosin II can be activated by extrinsic pathways when $cPLA_2$ signaling is inhibited and remains competent to bind to the cell cortex.

Recent work identified that the activation of proinflammatory signaling during leukocyte recruitment to wounding sites is regulated by tension-sensitive binding of $cPLA_2$ to the INM (*39*). We thus tested a role of $cPLA_2$ in the nucleus by generating a modified $cPLA_2$

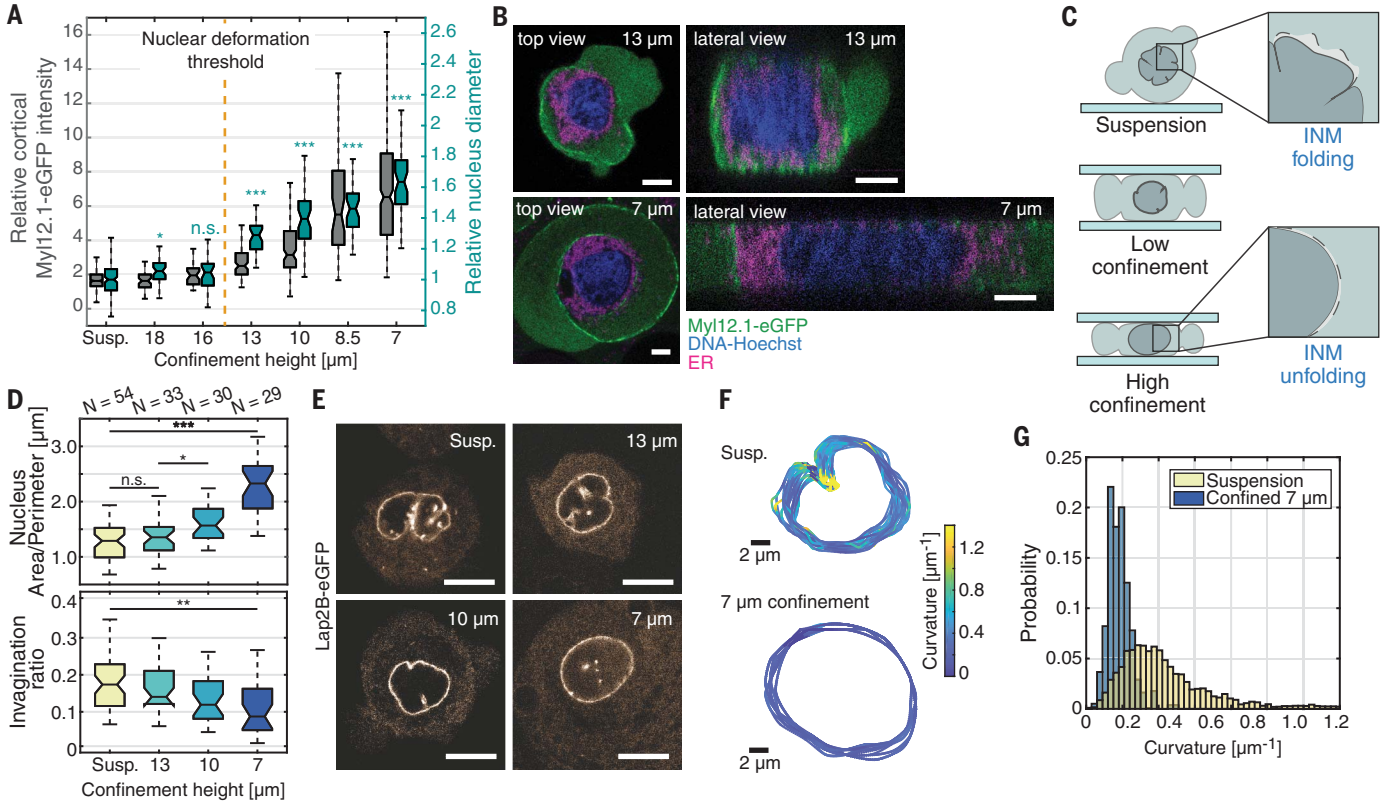

Fig. 3. Nuclear envelope unfolding is associated with increasing cortical contractility. (**A**) Double boxplot of relative cortical myosin II enrichment (left axis, gray) and relative nuclear diameter (right axis, teal) for decreasing confinement height. Statistical test for relative nuclear diameter performed with respect to suspension [*N* =144 cells (suspension); *N* = 44 (18 µm); *N* = 32 (16 µm); *N* = 37 (13 µm); *N* = 45 (10 µm); *N* = 37 (8.5 µm); *N* = 50 (7 µm)]. Statistical tests for cortical myosin II levels and experimental *N* related to Fig. 1A. (**B**) Exemplary confocal top views (*x*-*y*) and lateral views (*y*-*z*) of progenitor stem cells expressing myosin II–eGFP stained with DNA-Hoechst and ER-TrackerRed in 13 and 7 µm confinement. (**C**) Illustration showing the unfolding of the inner nuclear membrane (INM) with increasing cell confinement. (**D**) Nuclear area–to–perimeter ratio (top) and nuclear invagination ratio (bottom) for increasing confinement. (**E**) Exemplary confocal images of cells expressing Lap2B-eGFP under varying cell deformation. (**F**) Curvature analysis of nuclear shape for 20 consecutive frames (t_{lag} = 10 s) for unconfined (suspension, top) and 7 µm confined nuclei (bottom). (**G**) Histogram of nuclear curvature for unconfined and 7 µm confined nuclei related to (F) with *N* = 10 cells for each condition ($P < 10^{-12}$). ***P < 0.0001, **P < 0.001, *P < 0.01. Scale bar in (B), 5 µm; all other scale bars, 10 µm.

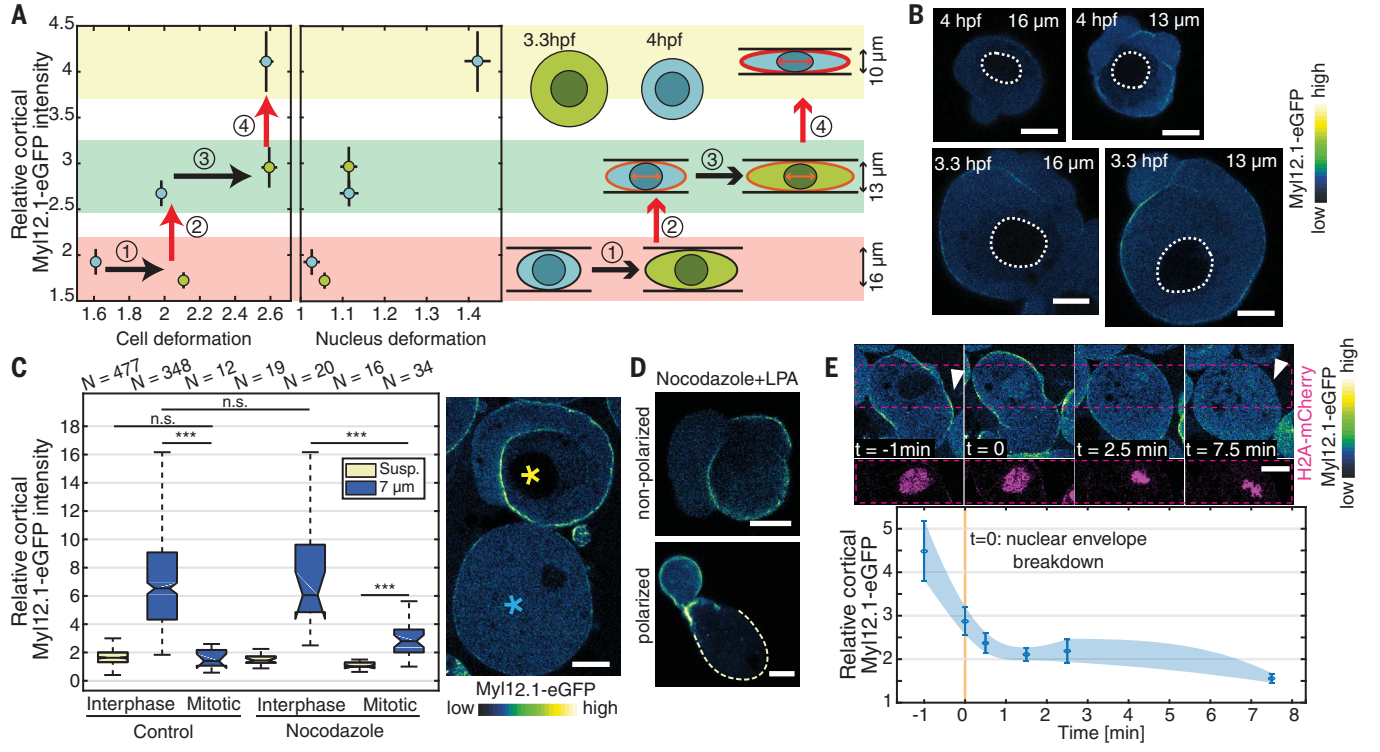

Fig. 4. Nucleus size and integrity determine the morphodynamic cell response to confinement. (**A**) Relative cortical myosin II intensity with respect to cell deformation as defined by the ratio of cell size to confinement height (left) and nucleus deformation (right) measured via relative nucleus diameter increase (right) for cells dissociated from embryos at high-oblong (3.3 hpf) and sphere (4 hpf) stage and cultured under similar confinement heights, as indicated. Data points and error bars indicate mean and SEM; 3.3 hpf: $N = 58$ (16 µm), $N = 61$ (13 µm); 4 hpf: $N = 44$ (16 µm), $N = 60$ (13 µm), $N = 45$ (10 µm). The Pearson correlation coefficient between myosin II intensity and nuclear deformation is 0.48. (**B**) Exemplary confocal images of progenitor cells expressing myosin II–eGFP under 16 and 13 µm confinement dissociated from 4 hpf (top) and 3.3 hpf (bottom) embryos. Dashed lines outline cell nuclei. (**C**) Relative cortical myosin II enrichment for interphase and mitotic cells under 7 µm confinement cultured in suspension (control) in the presence of 1 µM nocodazole. Exemplary confocal images of progenitor cells expressing myosin II–eGFP in interphase (yellow asterisk) or during mitosis (cyan asterisk) under 7 µm confinement. (**D**) Exemplary confocal images of progenitor unpolarized (top) and polarized (bottom) cells expressing myosin II–eGFP during mitosis treated with 1 µM nocodazole and 50 µM LPA. Dashed line shows the stable-bleb cell front. (**E**) Cortical myosin II intensity of $N = 7$ cells undergoing mitosis, and representative confocal time-lapse images of cells expressing myosin II–eGFP and H2A-mCherry at indicated time points ($t = 0$, time of nuclear envelope breakdown). The arrows point to the cell cortex with cortical myosin II enrichment ($t = -1$ min) or loss of cortical myosin II levels ($t = 7.5$ min). Data points and error bars indicate mean and SEM. ***$P < 0.0001$. All scale bars, 10 µm.

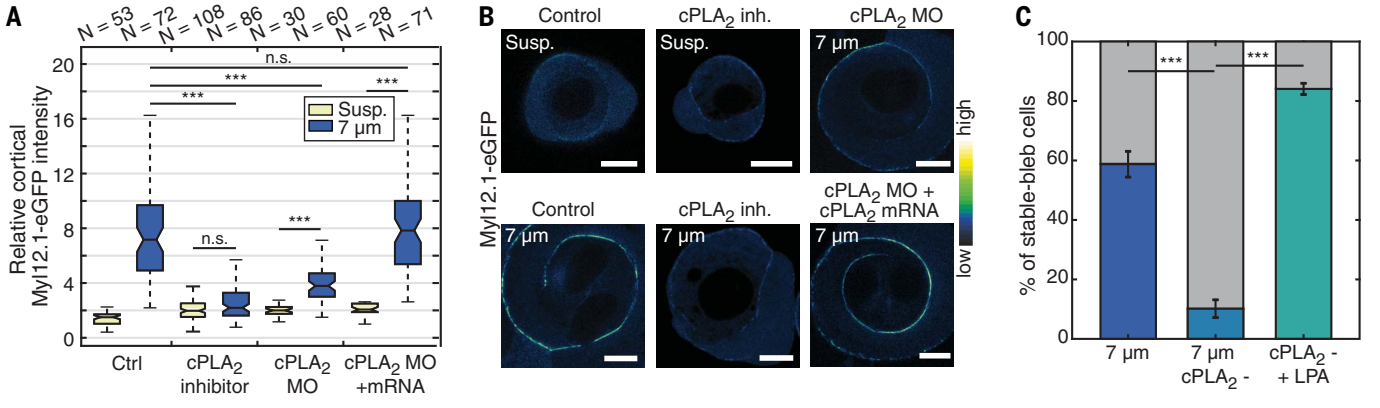

Fig. 5. Nucleus deformation activates a mechanosensitive lipase signaling pathway regulating myosin II activity. (**A**) Relative cortical myosin II intensity for progenitor cells cultured in suspension versus 7 µm confinement conditions for control cells (DMEM), with $cPLA_2$ inhibitor, or injected with $cPLA_2$ MO and $cPLA_2$ MO + $cPLA_2$ mRNA. (**B**) Exemplary confocal images of progenitor cells expressing myosin II–eGFP related to (A) for indicated conditions. (**C**) Percentage of stable-bleb polarized cells for control cells under 7 µm confinement and in the presence of $cPLA_2$ inhibitor or unconfined (suspension) cells stimulated with 50 µM LPA. For all conditions, $N > 200$ cells. ***$P < 0.0001$. All scale bars, 10 µm.

construct containing a nuclear export sequence (NES). Using leptomycin B as a blocker of nuclear export, we observed an accumulation of $cPLA_2$-NES-GFP within the nucleus, showing a concomitant increase of cortical myosin II levels in confined cells (Fig. 6, A and B). These data support that $cPLA_2$ localization in the nucleus is required for myosin II enrichment at the cortex.

We further validated that cortical myosin II enrichment in cells of different sizes (early versus late blastula cells) and different embryonic cell lineages (mesendoderm or ectoderm cells) depends on the activation of $cPLA_2$ signaling. Pharmacological inhibition of $cPLA_2$ activity blocked cortical myosin II relocalization in confined cells (Fig. 6C) and strongly reduced cell polarization and associated migration competence (fig. S2B), supporting a consistent role of $cPLA_2$ activation under physical cell deformation across early to late developmental stages. These data support that activation of $cPLA_2$ signaling in the nucleus mediates adaptive cytoskeletal and morphodynamic behavior under cell deformation.

Arachidonic acid (AA) is the primary cleavage product generated by $cPLA_2$ activity (*40*). To directly validate whether nucleus deformation in confinement triggers $cPLA_2$ activity, we measured the release of AA by Raman spectroscopy. The analysis of Raman spectra confirmed the specific production of AA in confined cells (Fig. 6D and fig. S5E), with the increase in AA production in confined versus control cells being specifically blocked in the presence of $cPLA_2$ inhibitor (Fig. 6E). We further observed that AA was exclusively detected in the cytoplasm of confined cells, which suggests that AA is directly released from nuclear membranes into the cytoplasm. These data support that cell confinement leads to enhanced $cPLA_2$ activity and production of AA associated with INM unfolding and stretching of the nucleus surface.

AA has been implicated in both the direct (*41*) and indirect regulation of myosin II activity via protein phosphorylation (*42*). We tested the involvement of the Rho/ROCK and myosin light chain kinase (MLCK) as key regulators of myosin II activity (*4*). MLCK inhibition showed no significant effect on myosin II enrichment in confined cells, whereas a pronounced reduction of cortical myosin II recruitment was observed when using staurosporine, a general kinase inhibitor, and under specific inhibition of Rho activity (Fig. 6F). Using a RhoA–Förster resonance energy transfer (FRET) sensor further indicated an increased RhoA activity in confined cells versus control cells in suspension, which was significantly reduced in the presence of $cPLA_2$ inhibitor in confined cells (fig. S5F). These data support that AA production by $cPLA_2$ activity initiates upon nuclear envelope unfolding, regulating phosphorylation-dependent myosin II activity at the cell cortex. AA and its metabolic products have been widely implicated in para- and autocrine signaling functions involving G protein–coupled receptors (*43*). We assessed the role of AA product release by compressing cells directly under micropillars at a height of ~7 μm, leading to confined and nonconfined cells in close proximity (fig. S5G). Whereas confined cells showed high levels of cortical myosin II and amoeboid cell transformation, nonconfined cells in direct contact revealed no alterations in cortical myosin II and cellular morphodynamics (fig. S5H). These results support that $cPLA_2$-dependent myosin II activation does not depend on the release of diffusible signals and regulates cellular

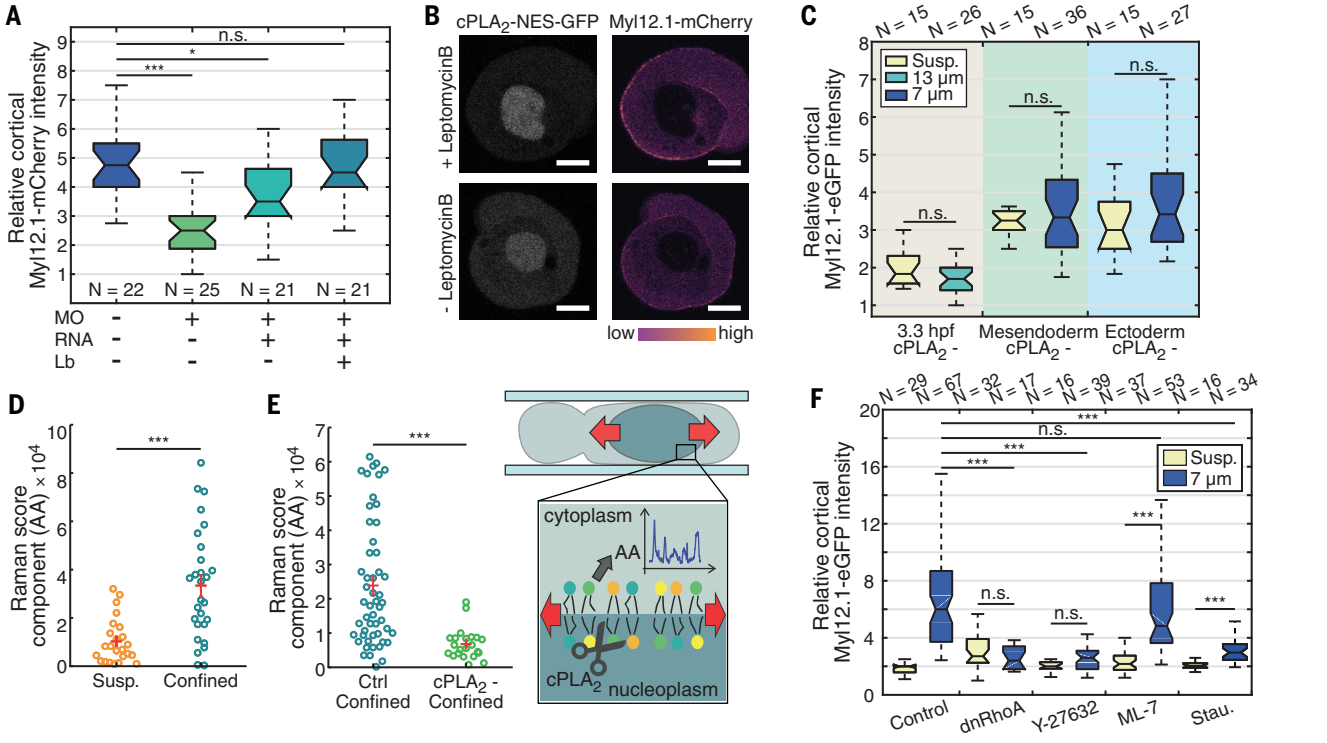

Fig. 6. cPLA2 activity at the inner nuclear membrane generates AA as a metabolite regulating cortical contractility in confinement. (**A**) Relative cortical myosin II fluorescence intensity for cells dissociated from controls (uninjected) embryos or embryos injected with $cPLA_2$ MO, $cPLA_2$ MO + $cPLA_2$-NES-GFP mRNA (RNA) and with or without addition of leptomycin B (Lb). (**B**) Exemplary confocal fluorescence images of cell expressing myosin II–mCherry (right) and $cPLA_2$-NES-GFP (left) under 7 μm confinement with (top) or without (bottom) the addition of Lb. (**C**) Relative cortical myosin II fluorescence intensity upon $cPLA_2$ inhibition for cells dissociated at 3.3 hpf, induced mesendoderm, or ectoderm cells in suspension and upon confinement at indicated height. (**D** and **E**) Scores of Raman component associated to AA in (D) suspension (unconfined, $N = 24$) and confined cells (10 μm, $N = 28$) and (E) in control confinement condition (Ctrl, $N = 52$) or treated with $cPLA_2$ inhibitor ($N = 22$). Red lines indicate mean and SEM. (**F**) Relative cortical myosin II intensity for control cells and different chemical (Y-27637, M-L7, staurosporine) or genetic interference [dominant negative RhoA (dnRhoA)] with myosin II regulators. ***$P < 0.0001$, *$P < 0.01$. All scale bars, 10 μm.

morphodynamics via a cell-autonomous increase of cortical contractility under cell deformation in confinement.

Interference with intracellular calcium levels by addition of BAPTA-AM [1,2-bis(2-aminophenoxy)ethane-*N*,*N*,*N*′,*N*′-tetraacetic acid acetoxymethyl ester] or in combination with $cPLA_2$ inhibitor blocked myosin II enrichment in confined cells without altering cortical myosin II levels in unconfined control cells (fig. S5I). LPA stimulation of BAPTA-AM–treated cells confirmed that myosin II can be activated by the Rho-ROCK signaling pathway in the absence of intracellular calcium and remains competent to bind the cell cortex (fig. S5C). Similarly, chelating extracellular calcium reduced cortical myosin II relocalization, while depletion of internal calcium stores using thapsigargin led to a slight increase in myosin II enrichment in confinement (fig. S5I). The addition of ionomycin showed that high intracellular calcium levels, in the absence of cellular shape deformation, were not sufficient to evoke AA production (fig. S5J) and cortical myosin II enrichment (fig. S5, B and D). This suggests that intracellular calcium has a permissive function for $cPLA_2$ association with the INM and increasing cortical contractility under cell confinement. Our findings are in line with the observation that $cPLA_2$ contains a calcium-dependent C2 domain that modulates protein binding to the INM (*44*–*46*), which has been shown to be further enhanced and stabilized by mechanical stretching of the nucleus (*39*). Consistently, $cPLA_2$ showed a transient localization to the INM in the presence of ionomycin, while additional mechanical stretch due to hypotonic swelling or cell confinement induced a stable association with the INM (fig. S3, J and K).

INM unfolding and nucleus positioning enable the decoding of different types of cell shape deformations

To study whether INM unfolding under cell confinement was sufficient to trigger $cPLA_2$ activity, we measured cortical myosin II levels and amoeboid migration competence under hypotonic swelling of cells. Quantification of nuclear shape parameters (size, volume, and surface) revealed that hypotonic swelling induced comparable nuclear surface expansion and INM unfolding as nucleus deformation under a confinement height of 7 μm (fig. S6, A to C). Cortical myosin II levels in hypotonic conditions (Fig. 7A and movie S7) and associated changes in bleb size (fig. S6D) and cell polarization rate (Fig. 7C) were significantly lower than those of cells deformed at a 7 μm confinement height. These observations suggest that nuclear envelope unfolding alone is not sufficient to trigger high levels of cortical myosin II enrichment under isotropic cell stretching in hypotonic conditions versus anisotropic cell deformation in confinement.

Comparing intracellular calcium levels between deformed cells in confinement and under hypotonic conditions showed a pronounced increase in intracellular calcium concentrations in confined cells, with a specific calcium increase in the cell nucleus (Fig. 7B and fig. S6E). Ectopically increasing intracellular calcium levels under hypotonic conditions via the addition of ionomycin led to a pronounced and rapid increase in cortical myosin II enrichment in a $cPLA_2$-dependent manner (fig. S6F and movie S7) that triggered spontaneous cell polarization (Fig. 7, C and D, and fig. S6G). As in confined cells, cell polarization under this condition was associated with a rapid transformation of nonmotile cells into a highly motile stable-bleb amoeboid mode with fast migration speed under confinement ex vivo

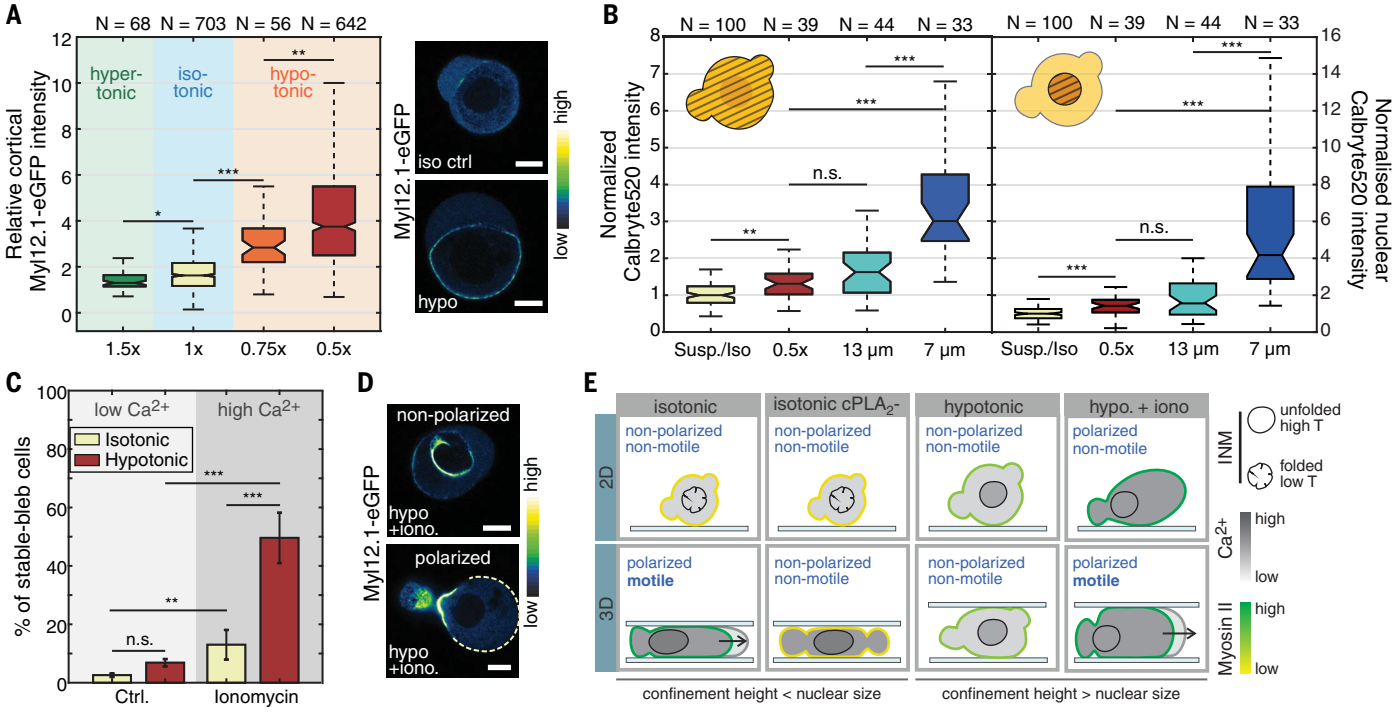

Fig. 7. Nucleus stretch and intracellular positioning enable an adaptive cellular response to different types of physical cell deformation. (**A**) Relative cortical myosin II enrichment for progenitor cells cultured under different osmolarity conditions. (**B**) Normalized cell (left) and nuclear (right) Ca^{2+} levels (Calbryte520) for control (Ctrl) and hypotonic (0.5×) conditions and mechanical confinement (13 and 7 μm). (**C**) Percentage of stable-bleb polarized cells in isotonic and hypotonic (0.5×) conditions for cells cultured in DMEM (Ctrl) or supplemented with 1 μM ionomycin. $N > 1000$ cells for all conditions. (**D**) Exemplary confocal images of cells expressing myosin II–eGFP in isotonic (ctrl, top left), hypotonic (bottom left) and hypotonic conditions supplemented with ionomycin treatment (right): nonpolarized cell (top) and stable-bleb polarized cell (bottom). (**E**) Sketch of cell polarization and motile cell behavior in 2D (top) versus 3D confined environments (bottom) and for control conditions (isotonic media; first column) versus $cPLA_2$ interference (second column) and hypotonic condition alone (third column) or in the presence of ionomycin (fourth column). high T, high tension; low T, low tension. ***$P < 0.0001$, **$P < 0.001$, *$P < 0.01$. All scale bars, 10 μm.

and in vivo (Fig. 7E; fig. S6, H, I, and M; and movies S7 and S8). Raman spectroscopy to directly measure $cPLA_2$ activity confirmed that hypotonic stress increased AA levels (fig. S5K) in a $cPLA_2$-dependent manner (fig. S5L), with addition of ionomycin in hypotonic conditions further increasing AA production (fig. S5M). Furthermore, relative measured AA levels directly correlated with cortical myosin II levels (fig. S5N). Together, these data reveal that different mechanical shape deformations regulate intracellular calcium levels and modulate $cPLA_2$ activity under similar INM stretch; uniaxial compression in confinement induces high intracellular calcium levels specifically in the nucleus, while isotropic radial stretch in hypotonic stress conditions leads to a lower intracellular calcium levels. Independently modulating nucleus deformation and calcium levels under different shape deformations confirmed that both parameters engage synergistically to regulate cortical contractility (Fig. 8A) and cellular dynamics under anisotropic stress (Fig. 7E), thereby enabling a cell to distinguish between different types of shape deformation and to acquire a specific morphodynamic response.

Intracellular nucleus positioning appeared as a promising candidate to differentially modulate calcium levels. Endoplasmic reticulum–plasma membrane (ER-PM) proximity has been implicated as an important regulator of cellular calcium signaling (*47*). Visualization of membrane-proximal ER structures showed that the ER was highly dynamic under conditions of low confinement but was increasingly immobilized between the nucleus-PM interface for larger cell deformations in confinement (movie S9). In addition, the expanding nucleus contact area close to the plasma membrane closely correlated with an intracellular calcium increase (fig. S6J). We speculated that stromal interaction molecule–Orai (STIM-Orai), with STIM proteins located at the ER and Orai proteins representing calcium-selective PM calcium channels, could be involved in cellular calcium regulation in confined cells. STIM-Orai proteins have an established function in store-operated calcium entry upon depletion of calcium from the ER, which is mediated via ER-PM proximity (*48*, *49*). Analysis of STIM-Orai protein localization revealed that both proteins accumulate at the interface between the nucleus and plasma membrane in confined cells at 7 μm (fig. S6, K and L). In contrast, we observed a homogeneous distribution of both channels in cells under 13 μm confinement height when the ER was not spatially confined between the nucleus and PM. These data support that ER immobilization is associated with the specific enrichment of STIM-Orai in the ER-PM contact region where mechanical ER confinement occurs. Inhibition of the STIM-Orai complex using 2-aminoethoxydiphenyl borate (2APB) further blocked myosin II enrichment under cell deformation in confinement (fig. S5I). Our observations support that mechanical compression of the cell nucleus induces a tight connectivity between ER-PM structures and STIM-Orai localization at the ER-PM contact interface involved in the up-regulation of intracellular calcium levels in confined cells.

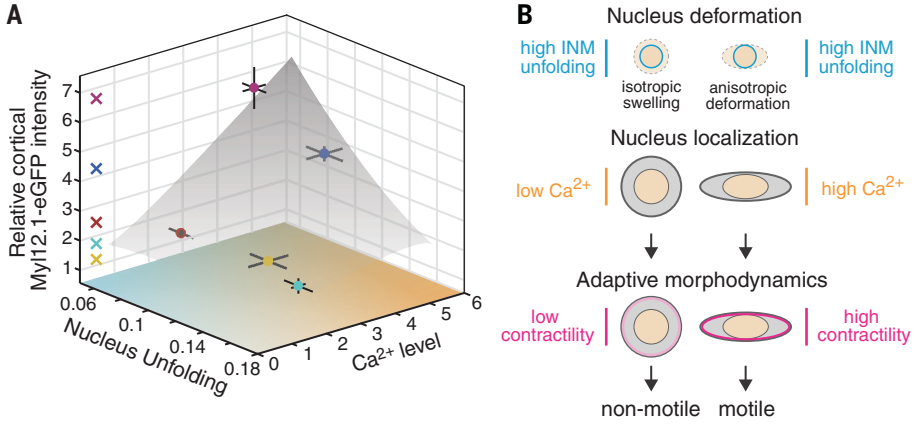

Fig. 8. INM unfolding and intracellular calcium levels enable cells to decode isotropic stretch versus cell squeezing in confinement. (**A**) Normalized relative cortical myosin II fluorescence intensity as a function of nucleus unfolding and normalized Ca^{2+} (Calbryte520) intensity for different physical cell deformations [dark blue, 7 μm confinement; light blue, 13 μm confinement; yellow, 7 μm confinement + BAPTA-AM; red, hypotonic (0.5×) condition; magenta, hypotonic condition (0.5×) + ionomycin]. Data indicate mean and SEM. The gray area sketches the relation between cortical myosin II and nuclear deformation versus intracellular calcium levels. [Calcium data related to Fig. 4B, except for hypo + ionomycin (N = 41) and BAPTA-AM + 7 μm (N = 9); for nuclear unfolding related to Fig. 2D and fig. S6B, and for cortical myosin II levels related to Figs. 1A and 4A and figs. S5I and S6F]. (**B**) Sketch depicting how nucleus deformation and intracellular nucleus positioning correlate with INM unfolding and intracellular calcium levels, which differentially regulate cortical contractility and cellular morphodynamics.

Discussion

Our data support that the nucleus establishes a core element to measure cellular shape deformation via two key physical parameters: (i) nuclear shape deformation leading to INM unfolding and (ii) intracellular spatial positioning of the nucleus. In this model, INM unfolding under nuclear shape change allows for the deformation-dependent activation of $cPLA_2$ signaling, whereby $cPLA_2$ activity is modulated by intracellular calcium levels set by nucleus-PM proximity (Fig. 8B and fig. S7A). The parameter space of these two variables (INM unfolding and calcium levels) provides a dual-input identifier for a cell to decode distinct shape deformations as exemplified on anisotropic cell deformation in confinement versus isotropic hypotonic cell stretching, allowing cells to acquire a specific adaptive response depending on the type of physical shape deformation (fig. S7B).

Biochemical, physical, and mechanical cues in the surrounding of a cell create manifold information for cells, which is continuously sensed, integrated, and transduced to allow for complex cellular functioning. Here, we show that the cell nucleus functions as a cellular mechano-gauge for precisely decoding cellular shape changes, allowing cells to adaptively and rapidly tune cytoskeletal network properties and morphodynamic behavior within their 3D tissue microenvironment during development. This mechanism lays a foundation for functional principles underlying cellular proprioception that, comparable to the sensing of spatiotemporal changes in body posture and movement (*50*), enable a precise interpretation of shape changes on the single-cell level.

The nucleus, being the largest organelle in the cell, represents a prominent structure for transmission and modulation of mechanosensitive processes (*51*–*55*), and nucleus deformation has been shown to influence nuclear transport and cell differentiation (*56*–*58*), chromatin organization (*59*–*61*), migration (*62*–*66*), and pathfinding in constrained environments (*67*). Our findings support that nucleus deformation and its intracellular positioning establish a cellular sensing module that equips cells to rapidly and reversibly adapt their dynamic response to shape fluctuations. This "nuclear ruler pathway" was also identified in an accompanying study (*68*), supporting its conservation between embryonic and differentiated cells in the adult organism. The observation of a rapid contractile cell response upon cell squeezing in confinement which is followed by fast amoeboid motility is reminiscent of a "cellular escape reflex" that enables cells to cope with physical constraints and acute

deformations of their shape. Such a mechanism might be relevant for various biological processes associated with migration plasticity of cancer and immune cells in constrained 3D tissue niches (*69*–*72*), mechanochemical feedback processes during morphogenesis (*73*), and homeostatic tissue functions such as cell density regulation (*74*), which require accurate mechanisms to detect variations in cellular size and shape and multicellular packing density in crowded 3D tissues.

Materials and methods

Zebrafish maintenance

Zebrafish (*Danio rerio*) were maintained as previously described (*75*). Embryos were kept in E3 medium at between 25° and 31°C before experiments and staged according to morphological criteria (*76*) and hours post-fertilization (hpf). Wild-type embryos were obtained from the AB strain background. All protocols used have been approved by the Institutional Animal Care and Use Ethic Committee (PRBB–IACUEC) and implemented according to national and European regulations. All experiments were carried out in accordance with the principles of the 3Rs (replacement, reduction, and refinement).

Transgenic fish lines

The following transgenic lines were used: Tg(actb2:Lifeact-GFP) (*77*), Tg(actb2:Myl12.1-eGFP) (*78*), Tg(actb2:Myl12.1-mcherry) (*4*), Tg(mezzo:eGFP) (*23*), and Tg(actb2:Lyn-TdTomato) (*79*). All progenitor cells expressing Myl12.1-eGFP (myosin II) and Lifeact-GFP (actin) were obtained from Tg(actb2:Myl12.1-eGFP) and Tg(actb2:Lifeact-GFP).

Cell culture

To culture progenitor cells, embryos were manually dechorionated in E3 buffer at sphere stage (4 hpf) or different stages, if indicated. Five to twenty embryos were transferred to Dulbecco's minimum essential medium–nutrient mixture F-12 (DMEM-F12; with L-glutamine and 15 mM HEPES, without sodium bicarbonate and phenol red) culture medium (Sigma) and mechanically dissociated by manual tapping followed by centrifugation at 200*g* for 3 min.

Sample preparation and surface coatings

The following products for surface coatings at the indicated concentration have been used: 0.5 mg/ml PLL(20)-g[3,5]-PEG(2) (Susos) and 0.2 mg/ml fibronectin (Sigma-Aldrich). Before PLL-PEG coating, both coverslips and dishes were plasma cleaned. Uncoated or PLL-coated glass dishes #1.5 were purchased from MatTek (MatTek Corporation).

Cell confiner

Cells were confined using a dynamic confiner (4DCell) similar to previously established planar microconfinement methods (*30*). To confine cells at different heights, multiple Si molds were produced by photolithography in a clean room (Nanofabrication Laboratory, ICFO) by depositing a SU-8 resin on a silicon wafer. In brief, a photomask with the desired geometry was created. Confinement coverslips were prepared with polydimethylsiloxane (PDMS) with the following heights: 18, 16, 13, 10, 8.5, and 7 μm. Coverslips were always plasma cleaned, coated with PLL-PEG (if not indicated otherwise), and equilibrated in DMEM before each experiment. A pressure pump (AF1 microfluidic pressure pump, Elveflow) together with the ESI software was used to change the pressure for tuning the confinement heights. For Raman measurements and optical tweezers, two coverslips separated with microbeads or with a PDMS membrane were used (height = 10 μm).

Reagents and inhibitor treatments

Pharmacological inhibitors were used at the following concentrations: 1 μM $cPLA_2$ inhibitor (pyrrophenone, Merck-Millipore), 10 μM Bapta-AM (Cayman), 10 μM blebbistatin(+) (Tocris Bioscience), 10 μM Y-27632 (Tocris Bioscience), 10 μM ML-7 hydrochloride (Tocris Bioscience), 1 μM nocodazole (Sigma), 50 nM leptomycinB (Sigma-Aldrich), 1 μM ionomycin (Sigma-Aldrich), 1 μM thapsigargin (Thermo Fisher), 10 μM GsMTx4 (Tocris), 50 μM 2-APB (Biogen-Santa Cruz), 10 μM gadolinium chloride (Tocris), 2 μM actinomycin D (PanReac), 100 μM Z-VAD(OMe)-FMK (Abcam), 1 μM staurosporine (Abcam), and 1-oleoyl lysophosphatidic acid (LPA, Tocris Bioscience). Measurements were done directly after exposure to MLCK inhibitor, GsMTx4, ionomycin, and LPA; all other inhibitors were preincubated for 30 and 60 min for Y-27632 prior to experiments.

Fluorescence staining

Calbryte520 (AAT Bioquest) was used to study calcium dynamics. The staining kit–Red Fluorescence–Cytopainter (ER Tracker, Abcam) or ER-Tracker Green (BODIPY FL Glibenclamide) was used to visualize the endoplasmic reticulum respectively for confocal 3D colors imaging and for TIRF microscopy experiment. DNA-Hoechst (Thermo Fisher) was used to stain the cell nucleus. Cells were incubated with 5 μM Calbryte520 for 20 min, with 1 μM ER-tracker for 30 min and 1 μg/ml DNA-Hoechst for 7 to 10 min, as reported in the corresponding protocols. After incubation, cells were washed, centrifuged at 200*g* for 3 min and resuspended in DMEM media.

Variable osmotic culture conditions

D-Mannitol (Sigma) was diluted in DMEM to obtain a culture medium with an osmolarity of ~450 milliosmoles per liter (corresponding to a 1.5× media). Milli-Q water was added to DMEM for hypotonic conditions.

REFERENCES AND NOTES

1. G. Salbreux, G. Charras, E. Paluch, Actin cortex mechanics and cellular morphogenesis. *Trends Cell Biol.* **22**, 536–545 (2012). doi: 10.1016/j.tcb.2012.07.001; pmid: 22871642
2. N. W. Goehring, S. W. Grill, Cell polarity: Mechanochemical patterning. *Trends Cell Biol.* **23**, 72–80 (2013). doi: 10.1016/j.tcb.2012.10.009; pmid: 23182746
3. A. C. Callan-Jones, R. Voituriez, Actin flows in cell migration: From locomotion and polarity to trajectories. *Curr. Opin. Cell Biol.* **38**, 12–17 (2016). doi: 10.1016/j.ceb.2016.01.003; pmid: 26827283
4. M. Vicente-Manzanares, X. Ma, R. S. Adelstein, A. R. Horwitz, Non-muscle myosin II takes centre stage in cell adhesion and migration. *Nat. Rev. Mol. Cell Biol.* **10**, 778–790 (2009). doi: 10.1038/nrm2786; pmid: 19851336
5. M. A. Wozniak, C. S. Chen, Mechanotransduction in development: A growing role for contractility. *Nat. Rev. Mol. Cell Biol.* **10**, 34–43 (2009). doi: 10.1038/nrm2592; pmid: 19197330
6. T. Lecuit, P. F. Lenne, E. Munro, Force generation, transmission, and integration during cell and tissue morphogenesis. *Annu. Rev. Cell Dev. Biol.* **27**, 157–184 (2011). doi: 10.1146/annurev-cellbio-100109-104027; pmid: 21740231
7. E. M. Balzer *et al.*, Physical confinement alters tumor cell adhesion and migration phenotypes. *FASEB J.* **26**, 4045–4056 (2012). doi: 10.1096/fj.12-211441; pmid: 22707566
8. K. J. Sonnemann, W. M. Bement, Wound repair: Toward understanding and integration of single-cell and multicellular wound responses. *Annu. Rev. Cell Dev. Biol.* **27**, 237–263 (2011). doi: 10.1146/annurev-cellbio-092910-154251; pmid: 21721944
9. J. Briscoe, S. Small, Morphogen rules: Design principles of gradient-mediated embryo patterning. *Development* **142**, 3996–4009 (2015). doi: 10.1242/dev.129452; pmid: 26628090
10. G. Charras, E. Sahai, Physical influences of the extracellular environment on cell migration. *Nat. Rev. Mol. Cell Biol.* **15**, 813–824 (2014). doi: 10.1038/nrm3897; pmid: 25355506
11. P. Roca-Cusachs, R. Sunyer, X. Trepat, Mechanical guidance of cell migration: Lessons from chemotaxis. *Curr. Opin. Cell Biol.* **25**, 543–549 (2013). doi: 10.1016/j.ceb.2013.04.010; pmid: 23726023
12. M. Duda *et al.*, Polarization of myosin II refines tissue material properties to buffer mechanical stress. *Dev. Cell* **48**, 245–260.e7 (2019). doi: 10.1016/j.devcel.2018.12.020; pmid: 30695698
13. A. Sumi *et al.*, Adherens junction length during tissue contraction is controlled by the mechanosensitive activity of actomyosin and junctional recycling. *Dev. Cell* **47**, 453–463.e3 (2018). doi: 10.1016/j.devcel.2018.10.025; pmid: 30458138
14. J. Aureille *et al.*, Nuclear envelope deformation controls cell cycle progression in response to mechanical force. *EMBO Rep.* **20**, e48084 (2019). doi: 10.15252/embr.201948084; pmid: 31368207
15. S. A. Gudipaty *et al.*, Mechanical stretch triggers rapid epithelial cell division through Piezo1. *Nature* **543**, 118–121 (2017). doi: 10.1038/nature21407; pmid: 28199303
16. E. Marinari *et al.*, Live-cell delamination counterbalances epithelial growth to limit tissue overcrowding. *Nature* **484**, 542–545 (2012). doi: 10.1038/nature10984; pmid: 22504180
17. G. T. Eisenhoffer *et al.*, Crowding induces live cell extrusion to maintain homeostatic cell numbers in epithelia. *Nature* **484**, 546–549 (2012). doi: 10.1038/nature10999; pmid: 22504183
18. M. Georgouli *et al.*, Regional activation of myosin II in cancer cells drives tumor progression via a secretory cross-talk with the immune microenvironment. *Cell* **176**, 757–774.e23 (2019). doi: 10.1016/j.cell.2018.12.038; pmid: 30712866
19. J. H. Kim *et al.*, Mechanical tension drives cell membrane fusion. *Dev. Cell* **32**, 561–573 (2015). doi: 10.1016/j.devcel.2015.01.005; pmid: 25684354
20. T. Luo, K. Mohan, P. A. Iglesias, D. N. Robinson, Molecular mechanisms of cellular mechanosensing. *Nat. Mater.* **12**, 1064–1071 (2013). doi: 10.1038/nmat3772; pmid: 24141449
21. C. J. Cattin *et al.*, Mechanical control of mitotic progression in single animal cells. *Proc. Natl. Acad. Sci. U.S.A.* **112**, 11258–11263 (2015). doi: 10.1073/pnas.1502029112; pmid: 26305930
22. T. Lämmermann, M. Sixt, Mechanical modes of 'amoeboid' cell migration. *Curr. Opin. Cell Biol.* **21**, 636–644 (2009). doi: 10.1016/j.ceb.2009.05.003; pmid: 19523798

23. V. Ruprecht *et al*., Cortical contractility triggers a stochastic switch to fast amoeboid cell motility. *Cell* **160**, 673–685 (2015). doi: 10.1016/j.cell.2015.01.008; pmid: 25679761
24. J. S. Logue *et al*., Erk regulation of actin capping and bundling by Eps8 promotes cortex tension and leader bleb-based migration. *eLife* **4**, e08314 (2015). doi: 10.7554/eLife.08314; pmid: 26163656
25. A. W. Holle *et al*., Cancer cells invade confined microchannels via a self-directed mesenchymal-to-amoeboid transition. *Nano Lett.* **19**, 2280–2290 (2019). doi: 10.1021/acs.nanolett.8b04720; pmid: 30775927
26. T. Brunet, M. Albert, W. Roman, D. C. Spitzer, N. King, A flagellate-to-amoeboid switch in the closest living relatives of animals. bioRxiv 2020.06.26.171736 (28 June 2020); https://doi.org/10.1101/2020.06.26.171736.
27. M. Ibo, V. Srivastava, D. N. Robinson, Z. R. Gagnon, Cell blebbing in confined microfluidic environments. *PLOS ONE* **11**, e0163866 (2016). doi: 10.1371/journal.pone.0163866; pmid: 27706201
28. Y. J. Liu *et al*., Confinement and low adhesion induce fast amoeboid migration of slow mesenchymal cells. *Cell* **160**, 659–672 (2015). doi: 10.1016/j.cell.2015.01.007; pmid: 25679760
29. R. Zhao *et al*., Cell sensing and decision-making in confinement: The role of TRPM7 in a tug of war between hydraulic pressure and cross-sectional area. *Sci. Adv.* **5**, eaaw7243 (2019). doi: 10.1126/sciadv.aaw7243; pmid: 31355337
30. M. Le Berre, E. Zlotek-Zlotkiewicz, D. Bonazzi, F. Lautenschlaeger, M. Piel, Methods for two-dimensional cell confinement. *Methods Cell Biol.* **121**, 213–229 (2014). doi: 10.1016/B978-0-12-800281-0.00014-2; pmid: 24560512
31. M. Bergert *et al*., Force transmission during adhesion-independent migration. *Nat. Cell Biol.* **17**, 524–529 (2015). doi: 10.1038/ncb3134; pmid: 25774834
32. M. Krieg *et al*., Tensile forces govern germ-layer organization in zebrafish. *Nat. Cell Biol.* **10**, 429–436 (2008). doi: 10.1038/ncb1705; pmid: 18364700
33. L. Solnica-Krezel, D. S. Sepich, Gastrulation: Making and shaping germ layers. *Annu. Rev. Cell Dev. Biol.* **28**, 687–717 (2012). doi: 10.1146/annurev-cellbio-092910-154043; pmid: 22804578
34. A. D. Bershadsky, N. Q. Balaban, B. Geiger, Adhesion-dependent cell mechanosensitivity. *Annu. Rev. Cell Dev. Biol.* **19**, 677–695 (2003). doi: 10.1146/annurev.cellbio.19.111301.153011; pmid: 14570586
35. A. Saha *et al*., Determining physical properties of the cell cortex. *Biophys. J.* **110**, 1421–1429 (2016). doi: 10.1016/j.bpj.2016.02.013; pmid: 27028651
36. W. C. Hung *et al*., Confinement sensing and signal optimization via Piezo1/PKA and myosin II pathways. *Cell Rep.* **15**, 1430–1441 (2016). doi: 10.1016/j.celrep.2016.04.035; pmid: 27160899
37. N. I. Petridou, S. Grigolon, G. Salbreux, E. Hannezo, C. P. Heisenberg, Fluidization-mediated tissue spreading by mitotic cell rounding and non-canonical Wnt signalling. *Nat. Cell Biol.* **21**, 169–178 (2019). doi: 10.1038/s41556-018-0247-4; pmid: 30559456
38. K. N. Dahl, S. M. Kahn, K. L. Wilson, D. E. Discher, The nuclear envelope lamina network has elasticity and a compressibility limit suggestive of a molecular shock absorber. *J. Cell Sci.* **117**, 4779–4786 (2004). doi: 10.1242/jcs.01357; pmid: 15331638
39. B. Enyedi, M. Jelcic, P. Niethammer, The cell nucleus serves as a mechanotransducer of tissue damage-induced inflammation. *Cell* **165**, 1160–1170 (2016). doi: 10.1016/j.cell.2016.04.016; pmid: 27203112
40. E. A. Dennis, J. Cao, Y. H. Hsu, V. Magrioti, G. Kokotos, Phospholipase A2 enzymes: Physical structure, biological function, disease implication, chemical inhibition, and therapeutic intervention. *Chem. Rev.* **111**, 6130–6185 (2011). doi: 10.1021/cr200085w; pmid: 21910409
41. T. Katayama *et al*., Stimulatory effects of arachidonic acid on myosin ATPase activity and contraction of smooth muscle via myosin motor domain. *Am. J. Physiol. Heart Circ. Physiol.* **298**, H505–H514 (2010). doi: 10.1152/ajpheart.00577.2009; pmid: 19933418
42. M. Brown, J. A. Roulson, C. A. Hart, T. Tawadros, N. W. Clarke, Arachidonic acid induction of Rho-mediated transendothelial migration in prostate cancer. *Br. J. Cancer* **110**, 2099–2108 (2014). doi: 10.1038/bjc.2014.99; pmid: 24595005
43. L. Sun, R. D. Ye, Role of G protein-coupled receptors in inflammation. *Acta Pharmacol. Sin.* **33**, 342–350 (2012). doi: 10.1038/aps.2011.200; pmid: 22367283
44. M. Peters-Golden, K. Song, T. Marshall, T. Brock, Translocation of cytosolic phospholipase A2 to the nuclear envelope elicits topographically localized phospholipid hydrolysis. *Biochem. J.* **318**, 797–803 (1996). doi: 10.1042/bj3180797; pmid: 8836122
45. A. Dessen *et al*., Crystal structure of human cytosolic phospholipase A2 reveals a novel topology and catalytic mechanism. *Cell* **97**, 349–360 (1999). doi: 10.1016/S0092-8674(00)80744-8; pmid: 10319815
46. J. E. Burke, E. A. Dennis, Phospholipase A_2 biochemistry. *Cardiovasc. Drugs Ther.* **23**, 49–59 (2009). doi: 10.1007/s10557-008-6132-9; pmid: 18931897
47. A. Gallo, C. Vannier, T. Galli, Endoplasmic reticulum-plasma membrane associations: Structures and functions. *Annu. Rev. Cell Dev. Biol.* **32**, 279–301 (2016). doi: 10.1146/annurev-cellbio-111315-125024; pmid: 27298092
48. S. Carrasco, T. Meyer, STIM proteins and the endoplasmic reticulum-plasma membrane junctions. *Annu. Rev. Biochem.* **80**, 973–1000 (2011). doi: 10.1146/annurev-biochem-061609-165311; pmid: 21548779
49. X. Qin *et al*., Increased confinement and polydispersity of STIM1 and Orai1 after Ca^{2+} store depletion. *Biophys. J.* **118**, 70–84 (2020). doi: 10.1016/j.bpj.2019.11.019; pmid: 31818466
50. R. Das, S. Wieser, M. Krieg, Neuronal stretch reception – Making sense of the mechanosense. *Exp. Cell Res.* **378**, 104–112 (2019). doi: 10.1016/j.yexcr.2019.01.028; pmid: 30817929
51. T. J. Kirby, J. Lammerding, Emerging views of the nucleus as a cellular mechanosensor. *Nat. Cell Biol.* **20**, 373–381 (2018). doi: 10.1038/s41556-018-0038-y; pmid: 29467443
52. Z. Jahed, M. R. Mofrad, The nucleus feels the force, LINCed in or not! *Curr. Opin. Cell Biol.* **58**, 114–119 (2019). doi: 10.1016/j.ceb.2019.02.012; pmid: 31002996
53. C. S. Janota, F. J. Calero-Cuenca, E. R. Gomes, The role of the cell nucleus in mechanotransduction. *Curr. Opin. Cell Biol.* **63**, 204–211 (2020). doi: 10.1016/j.ceb.2020.03.001; pmid: 32361559
54. R. P. Martins, J. D. Finan, G. Farshid, D. A. Lee, Mechanical regulation of nuclear structure and function. *Annu. Rev. Biomed. Eng.* **14**, 431–455 (2012). doi: 10.1146/annurev-bioeng-071910-124638; pmid: 22655599
55. Y. Xia, C. R. Pfeifer, S. Cho, D. E. Discher, J. Irianto, Nuclear mechanosensing. *Emerg Top Life Sci* **2**, 713–725 (2018). doi: 10.1042/ETLS20180051; pmid: 31693005
56. A. Elosegui-Artola *et al*., Force triggers YAP nuclear entry by regulating transport across nuclear pores. *Cell* **171**, 1397–1410.e14 (2017). doi: 10.1016/j.cell.2017.10.008; pmid: 29107331
57. J. Swift *et al*., Nuclear lamin-A scales with tissue stiffness and enhances matrix-directed differentiation. *Science* **341**, 1240104 (2013). doi: 10.1126/science.1240104; pmid: 23990565
58. M. Almonacid, M. E. Terret, M. H. Verlhac, Nuclear positioning as an integrator of cell fate. *Curr. Opin. Cell Biol.* **56**, 122–129 (2019). doi: 10.1016/j.ceb.2018.12.002; pmid: 30594054
59. K. Damodaran *et al*., Compressive force induces reversible chromatin condensation and cell geometry-dependent transcriptional response. *Mol. Biol. Cell* **29**, 3039–3051 (2018). doi: 10.1091/mbc.E18-04-0256; pmid: 30256731
60. A. Kumar *et al*., ATR mediates a checkpoint at the nuclear envelope in response to mechanical stress. *Cell* **158**, 633–646 (2014). doi: 10.1016/j.cell.2014.05.046; pmid: 25083873
61. M. M. Nava *et al*., Heterochromatin-driven nuclear softening protects the genome against mechanical stress-induced damage. *Cell* **181**, 800–817.e22 (2020). doi: 10.1016/j.cell.2020.03.052; pmid: 32302590
62. A. L. McGregor, C.-R. Hsia, J. Lammerding, Squish and squeeze — the nucleus as a physical barrier during migration in confined environments. *Curr. Opin. Cell Biol.* **40**, 32–40 (2016). doi: 10.1016/j.ceb.2016.01.011; pmid: 26895141
63. R. Majumdar, K. Steen, P. A. Coulombe, C. A. Parent, Non-canonical processes that shape the cell migration landscape. *Curr. Opin. Cell Biol.* **57**, 123–134 (2019). doi: 10.1016/j.ceb.2018.12.013; pmid: 30852463
64. R. J. Petrie, H. Koo, K. M. Yamada, Generation of compartmentalized pressure by a nuclear piston governs cell motility in a 3D matrix. *Science* **345**, 1062–1065 (2014). doi: 10.1126/science.1256965; pmid: 25170155
65. C. M. Denais *et al*., Nuclear envelope rupture and repair during cancer cell migration. *Science* **352**, 353–358 (2016). doi: 10.1126/science.aad7297; pmid: 27013428
66. M. Raab *et al*., ESCRT III repairs nuclear envelope ruptures during cell migration to limit DNA damage and cell death. *Science* **352**, 359–362 (2016). doi: 10.1126/science.aad7611; pmid: 27013426
67. J. Renkawitz *et al*., Nuclear positioning facilitates amoeboid migration along the path of least resistance. *Nature* **568**, 546–550 (2019). doi: 10.1038/s41586-019-1087-5; pmid: 30944468
68. A. J. Lomakin *et al*., The nucleus acts as a ruler tailoring cell responses to spatial constraints. *Science* **370**, eaba2894 (2020).
69. S. van Helvert, C. Storm, P. Friedl, Mechanoreciprocity in cell migration. *Nat. Cell Biol.* **20**, 8–20 (2018). doi: 10.1038/s41556-017-0012-0; pmid: 29269951
70. H. D. Moreau, M. Piel, R. Voituriez, A. M. Lennon-Duménil, Integrating physical and molecular insights on immune cell migration. *Trends Immunol.* **39**, 632–643 (2018). doi: 10.1016/j.it.2018.04.007; pmid: 29779848
71. V. te Boekhorst, L. Preziosi, P. Friedl, Plasticity of cell migration in vivo and in silico. *Annu. Rev. Cell Dev. Biol.* **32**, 491–526 (2016). doi: 10.1146/annurev-cellbio-111315-125201; pmid: 27576118
72. D. Wirtz, K. Konstantopoulos, P. C. Searson, The physics of cancer: The role of physical interactions and mechanical forces in metastasis. *Nat. Rev. Cancer* **11**, 512–522 (2011). doi: 10.1038/nrc3080; pmid: 21701513
73. E. Hannezo, C.-P. Heisenberg, mechanochemical feedback loops in development and disease. *Cell* **178**, 12–25 (2019). doi: 10.1016/j.cell.2019.05.052; pmid: 31251912
74. S. A. Gudipaty, J. Rosenblatt, Epithelial cell extrusion: Pathways and pathologies. *Semin. Cell Dev. Biol.* **67**, 132–140 (2017). doi: 10.1016/j.semcdb.2016.05.010; pmid: 27212253
75. W. Westerfield, *The Zebrafish Book: A Guide for the Laboratory Use of Zebrafish (Brachydanio rerio)* (Univ. of Oregon Press, 1995).
76. C. B. Kimmel, W. W. Ballard, S. R. Kimmel, B. Ullmann, T. F. Schilling, Stages of embryonic development of the zebrafish. *Dev. Dyn.* **203**, 253–310 (1995). doi: 10.1002/aja.1002030302; pmid: 8589427
77. M. Behrndt *et al*., Forces driving epithelial spreading in zebrafish gastrulation. *Science* **338**, 257–260 (2012). doi: 10.1126/science.1224143; pmid: 23066079
78. J. L. Maître *et al*., Adhesion functions in cell sorting by mechanically coupling the cortices of adhering cells. *Science* **338**, 253–256 (2012). doi: 10.1126/science.1225399; pmid: 22923438
79. J. Compagnon *et al*., The notochord breaks bilateral symmetry by controlling cell shapes in the zebrafish laterality organ. *Dev. Cell* **31**, 774–783 (2014). doi: 10.1016/j.devcel.2014.11.003; pmid: 25535919

ACKNOWLEDGMENTS

We acknowledge the Super-resolution Light Microcopy and Nanoscopy (SLN) Facility of ICFO for their support with imaging experiments and J. Osmond (Nanofabrication Laboratory, ICFO) for the design and production of molds for generating confinement coverslips, and further support from the CRG Core Facilities for Genomics and Advanced Light Microscopy. We thank the following labs that kindly provided plasmids: pCS2+ lefty/casanova (courtesy C.-P. Heisenberg); pCS2+ lyn-TdTomato (courtesy B. Alsina); pTriEx-RhoA FLARE.sc Biosensor WT was a gift from K. Hahn (Addgene plasmid #12150; RRID:Addgene_12150). We thank C.-P. Heisenberg, M. Piel, and A. J. Lomakin for discussions on this work and B. Lehner, V. Malhotra, S. P. Maurer, and the Ruprecht and Wieser lab members for critical reading of the manuscript. **Funding:** V.V. acknowledges support from the ICFOstepstone PhD Programme funded by the European Union's Horizon 2020 research and innovation program under Marie Skłodowska-Curie grant agreement 665884. F.P. and Q.T.-R. acknowledge grants funded by Ministerio de Ciencia, Innovación y Universidades and Fondo Social Europeo (FSE) (BES2017-080523-SO, PRE2018-084393). M.A.V. acknowledges support from the Spanish Ministry of Science, Education and Universities through grant RTI2018-099718-B-100 and an institutional "Maria de Maeztu Programme" for Units of Excellence in R&D (CEX2018-000792-M) and FEDER funds. J.W. was supported by the Christian Doppler Forschungsgesellschaft (Josef Ressel Center for Phytogenic Drug Research). S.W. and M.K. acknowledge support from the Spanish Ministry of Economy and Competitiveness through the Severo Ochoa program for Centres of Excellence in R&D (CEX2019-000910-S), from Fundació Privada Cellex, Fundación Mig-Puig, and from Generalitat de Catalunya through the CERCA program and LaserLab

(654148). M.K. acknowledges support through Spanish Ministry of Economy and Competitiveness (RYC-2015-17935, EQC2018-005048-P, AEI-010500-2018-228, and PGC2018-097882-A-I00), Generalitat de Catalunya (2017 SGR 1012), the ERC (715243), and the HFSPO (CDA00023/2018). S.W. acknowledges support through the Spanish Ministry of Economy and Competitiveness via MINECO's Plan Nacional (PGC2018-098532-A-I00). V.R. acknowledges support from the Spanish Ministry of Science and Innovation to the EMBL partnership, the Centro de Excelencia Severo Ochoa, the CERCA Programme/Generalitat de Catalunya, and the MINECO's Plan Nacional (BFU2017-86296-P). **Author contributions:** V.R. and S.W. designed the research. V.V. performed key experiments and data analysis. F.P. contributed to hypotonic and interference experiments and RNA preparations. F.C.C. and V.V. performed optical tweezer experiments, and F.C.C, analyzed the data. M.M. and V.V. performed Raman experiments, and M.M. analyzed the data. M.C.-R. analyzed the Lap2B-GFP data. H.-M.H. and Q.T.-R. performed in vivo experiments and H.-M.H. performed injections and helped with mesendoderm-ectoderm experiments. S.J.-D. cloned plasmids, synthetized mRNA. and performed mRNA and bead injections. S.P.-L. performed calcium imaging related to the role of Piezo channels. M.A.V. supervised S.P.-L. and contributed with discussions and support to calcium imaging experiments. J.W. provided biological reagents and supported molecular cloning. M.K. supervised F.C.C. and designed tweezer experiments. S.W. and V.R. supervised the project, contributed to data analysis, and wrote the manuscript. P.L.-A. supervised M.M. **Competing interests:** The authors declare no competing interests. **Data and materials availability:** All data relevant for the conclusions of this work are available in the main text or the supplementary materials.

SUPPLEMENTARY MATERIALS

science.sciencemag.org/content/370/6514/eaba2644/suppl/DC1
Supplementary Methods
Figs. S1 to S7
Table S1
References (*80*–*86*)
MDAR Reproducibility Checklist
Movies S1 to S9

View/request a protocol for this paper from *Bio-protocol*.

20 November 2019; resubmitted 29 June 2020
Accepted 28 August 2020
10.1126/science.aba2644

The nucleus measures shape changes for cellular proprioception to control dynamic cell behavior

Valeria Venturini, Fabio Pezzano, Frederic Català Castro, Hanna-Maria Häkkinen, Senda Jiménez-Delgado, Mariona Colomer-Rosell, Monica Marro, Queralt Tolosa-Ramon, Sonia Paz-López, Miguel A. Valverde, Julian Weghuber, Pablo Loza-Alvarez, Michael Krieg, Stefan Wieser and Verena Ruprecht

Science **370** (6514), eaba2644.
DOI: 10.1126/science.aba2644

The nucleus makes the rules

Single cells continuously experience and react to mechanical challenges in three-dimensional tissues. Spatial constraints in dense tissues, physical activity, and injury all impose changes in cell shape. How cells can measure shape deformations to ensure correct tissue development and homeostasis remains largely unknown (see the Perspective by Shen and Niethammer). Working independently, Venturini *et al.* and Lomakin *et al.* now show that the nucleus can act as an intracellular ruler to measure cellular shape variations. The nuclear envelope provides a gauge of cell deformation and activates a mechanotransduction pathway that controls actomyosin contractility and migration plasticity. The cell nucleus thereby allows cells to adapt their behavior to the local tissue microenvironment.

Science, this issue p. eaba2644, p. eaba2894; see also p. 295